Dynamic Simulation of Full Complement Cylindrical Roller Bearings with a Semi-Analytical Roller End-Flange Contact Detection Method

Marius Wolf[1], Arshia Fatemi[2]

[1] *Corporate Research, Robert Bosch GmbH Renningen, marius.wolf2@de.bosch.com*
[2] *Corporate Research, Robert Bosch GmbH Renningen, arshia.fatemi@de.bosch.com*

Abstract –
For cylindrical and tapered roller element bearings under axial load, the roller dynamics, damage mechanisms and efficiency are strongly impacted by roller end-flange contacts. Multibody simulation is a expedient tool to acquire insights in the influence of roller end-flange contacts on these effects. However, multibody simulation is only applicable in the development process, if the simulation tool has an appropriate runtime.
For an accurate physical model of the roller end-flange contact, it is essential to determine the contact's location and theoretical penetration. In order to increase numerical efficiency of the contact detection without compromising precision, a significantly faster and more stable semi-analytical approach for contact detection within multibody simulation has been developed [1].
In this paper, it is critically investigated how significant the runtime and stability advantages of the new contact detection algorithm [1] *are in context of an entire multibody simulation in comparison with full numerical models.*

[1] *Wolf, M., Sanner A. and Fatemi, A., 2020, "A Semi-Analytical Approach for Rapid Detection of Roller-Flange Contacts in Roller Element Bearings," Proc. Inst. Mech. Eng., Part J.*

Keywords – roller element bearings, roller end-flange contact, contact detection, multibody simulation, dynamic simulation, full complement cylindrical roller bearings, semi-analytical methods

1. Introduction

Dynamic behavior, efficiency and wear of axially loaded cylindrical and tapered roller element bearings (REBs) are strongly effected by normal and friction forces of the roller end-flange contact [2]. In addition, the governing physics of roller end-flange contacts are highly complex, therefore it is a current field of research [2-5].
The universal contact detection algorithms of commercial multibody software are usually not effective enough for specific contact simulation, concerning simulation time [6].
Normal force and radii of curvature are principal input quantities for physical modeling of roller end-flange contacts. These quantities are both functions of the theoretical penetration and location of the contact, which are calculated within the contact detection step. In addition, the resultant torque is highly dependent on the force application points.
However, for actual application of multibody dynamics simulations (MBS) in the development process of new bearings and products, enhanced simulation runtime is also an indispensable necessity besides high accuracy.

In literature, many approaches for contact detection at the roller end-flange interface can be found (see sect. 2). The authors recently developed a new semi-analytical algorithm for precise and efficient contact detection [1]. It was compared to state of the art contact detection methods and its runtime proved to be significantly faster in a laboratory-like environment.
Nevertheless, for physical modeling of normal and friction forces within a REB, a considerable amount of equations needs to be solved (see sect. 3) and integration of the equations of motion needs to be performed. Thus, contact detection is just one among many steps in the MBS of bearings. Therefore, the relative runtime advantages of the new approach [1] could be far less significant in case of actual application within a MBS. This motivates the investigation of the impact of contact detection algorithms on the overall (numerical) performance of dynamic simulation of REB.

In this paper, contact detection refers to determination of the contact location $\boldsymbol{P}_\mathrm{m}$ and theoretical rigid body penetration δ. The contact's location is the midpoint between the contact points $\boldsymbol{P}_i$ of each body:

$$\boldsymbol{P}_\mathrm{m} = \frac{\boldsymbol{P}_1 + \boldsymbol{P}_2}{2}. \qquad \textit{(Eq. 1)}$$

Contact points are always located on the body's outer surface and correspond to the pair of points with minimal distance, if the bodies are not in contact. If contact occurs, the contact points equal the pair of points with maximum penetration. A more precise definition is given by Wolf et al. [1].

2. Roller End-Flange Contact Detection Models

The following section provides a brief overview of the most relevant contact detection models, which are currently available. A more comprehensive review can be found in Wolf et al. [1].

Universal contact detection within commercial MBS programs is mostly based on discretization of the outer contour of bodies into polygons. Contact detection is then carried out, by checking interference for each polygon [6], [7].
While use of this intrinsic contact detection method is easily applied, it does neither fulfill the requirements concerning accuracy nor numerical efficiency.

In order to avoid the above mentioned drawbacks, Gupta [8] developed an approach based on discretization of roller end geometry as a torus and flange geometry as a cone. Theoretical penetration between these figures can be expressed as a function of the torus' angular coordinate. Contact location $\boldsymbol{P}_\mathrm{m}$ equals the location of maximum penetration. It can be determined using standard numerical schemes for finding extrema of a scalar functions.

Koch [9] introduces a comprehensive method based on gradients of the surface's implicit functions (gradient method). It allows for a variable detailed geometrical approximation by using spheres (SP), cones (CO), tori (TO) and polynomials as basic figures (see fig. 1).

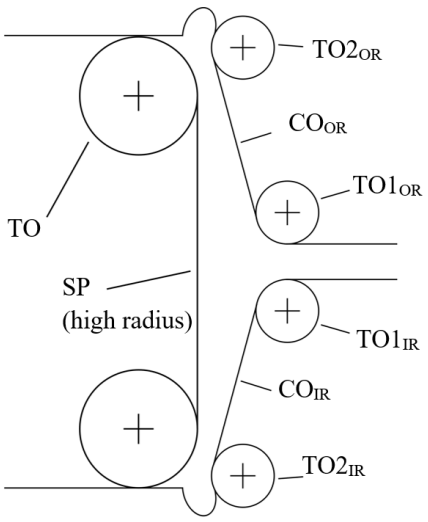

Figure 1: Schematic sketch of a possible roller end and flange geometric approximation at the inner ring (IR) and outer ring (OR).

Three conditions must be fulfilled for the contact points P_1 and P_2:

1. P_1 and P_2 must be located on the body's surface, defined by the implicit function F_i.
2. gradients of F_i must be collinear to each other at P_1 and P_2.
3. gradients of F_i must be collinear to the connecting vector between P_1 and P_2.

For better visualization of these conditions, contact points and gradients for a sphere-cone contact are shown in fig. 2. Eight scalar equations result from the conditions, which need to be solved for six coordinates of the contact points and two scaling factors resulting from the collinearity requirements. This non-linear system of equations is determined and must be solved iteratively.

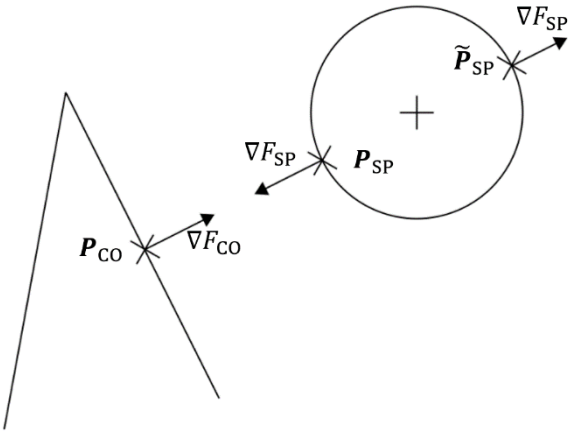

Figure 2: Schematic sketch of the gradient method constraints [9] for a sphere-cone contact. The constraints are fulfilled for all indicated points, yet only $\boldsymbol{P}_\mathrm{SP}$ corresponds to the sphere's actual contact point.

While this approach allows for a very precise approximation of the roller end and flange geometry, its convergence to the correct contact points is not guaranteed, as can be seen in fig. 2. $\boldsymbol{P}_\mathrm{SP}$ and $\widetilde{\boldsymbol{P}}_\mathrm{SP}$ both fulfill the conditions towards contact points, however only $\boldsymbol{P}_\mathrm{SP}$ equals the physical contact point. If the algorithm converges towards $\boldsymbol{P}_\mathrm{SP}$ or $\widetilde{\boldsymbol{P}}_\mathrm{SP}$, depends on the initial guess for iterative solving of the system of equations. Runtime of the gradient method can significantly be reduced within MBS, by storing the solution of the previous time step and using it as the initial guess of the current time step.

The authors recently developed a semi-analytical approach for contact detection in roller element bearings [1]. Analogous to Koch's gradient method [9], it uses a combination of spheres, cones and tori as basic figures to model the roller end and flange geometry as a piecewise function. Planes are represented by spheres with very high radii (see fig. 1). Analytical solutions were derived for sphere-sphere, sphere-cone and sphere-torus pairings. The main idea of the analytical solutions is reduction of the three-dimensional problem into a two-dimensional problem. It can be shown, that the contact points are always located within the plane defined by the sphere's center and rotational axis of the second geometrical figure. Inspection of the contact problem within this plane and the use of trigonometric functions then allows for solving the contact problem with analytical

equations.

Torus-cone contacts are handled similarly to Gupta [8], as described previously in this paper.

For torus-torus contacts, the first step is reduction of the two tori into circles defined by their major radii and determination of the minimal distance. A solution to finding the minimal distance between two arbitrarly located and orientated circles is given by Eberly [10] . Since the distance function is transferred into polynomial form, the global minimum can be determined numerically efficient without convergence issues.

It can be shown, that the actual contact points of the torus-torus problem correspond to the contact points of two spheres located at the contact points of the circle-cirlce problem with radii of the respective torus' minor radius. Finally, the contact points are calculated using the analytical equations derived for the sphere-sphere problem.

The semi-analytical approach [1] was compared to the gradient method of Koch [9] in a laboratory-like environment. In addition of being significantly faster (approx. 37 times), the semi-analytical approach also proved to yield an enhanced numerical stability compared to the gradient method.

3. Simulation Model

A six degree of freedom (DOF) model for simulation of the dynamic behavior of full-complement cylindrical REBs including lubrication was developed.

It allows modeling of dynamic radial and axial loads. Lubrication models for each contact based on rheological lubricant models have been incorporated in the model, since they are essential for the assessment of friction forces.

Normal and tangential forces are calculated for the roller-race, roller-roller and roller end-flange contacts of each roller. Rolling resistance is only considered for roller-race contacts, since roller-roller and roller end-flange contacts are dominated by sliding.

In case of cylindrical REBs, roller-race and roller-roller contacts can be approximated with line contacts. Tilting and skewing of rollers leads to an asymmetric pressure distribution at the contact. This effect and the shape of the rollers are considered by using a roller-slicing technique [11]. Contact detection and load calculation are performed for each slice. For normal and tangential load calculation, each slice is considered as an independent line contact.

The geometrical shape of roller end-flange contacts can vary greatly [2]. In this paper, it is approximated as an elliptical contact.

3.1. Normal Force $\boldsymbol{F}_\mathbf{n}$

3.1.1. Theoretical Penetration

In this paper, theoretical penetration refers to the rigid body penetration and equals the physical deflection at the contact. It is calculated within the contact detection step.

For roller end-flange contacts, the recently developed semi-analytical approach [1] and Koch's gradient method [9] for contact detection were implemented.

For roller-roller and roller-race contact detection, the roller slices and races are modelled as cylinders. Local vectors of the cylinders' geometrical center can be calculated dependent on skewing and tilting using standard geometrical functions.

For calculation of the contact location $\boldsymbol{P}_\mathrm{m}$ and theoretical penetration δ, it is assumed, that the cylinders representing rollers and races are parallel to each other. This allows for a simple analytical contact detection (see fig. 3):

$$\delta = \|\Delta \boldsymbol{r}_\perp\| - (R_1 + R_2) \qquad \textit{(Eq. 2)}$$

$$\boldsymbol{P}_\mathrm{m} = \boldsymbol{r_1} - \boldsymbol{\Delta r}_\perp \left(R_1 - \frac{\delta}{2}\right). \qquad \textit{(Eq. 3)}$$

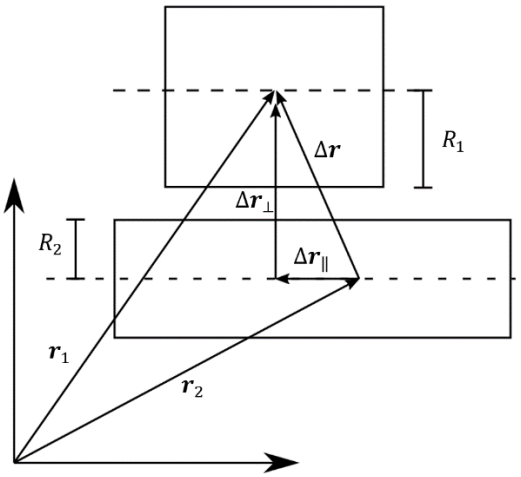

Figure 3: Schematic sketch of generic contact detection for two parallel cylinders.

The assumption of parallel cylinders is valid, since skew and tilt angles are relatively small in cylindrical REBs.

Theoretical penetration is then used in load-deflection relationships to calculate the normal load of each contact (elliptical) or slice (line).

3.1.2. Elliptical Contacts at Roller End-Flange Interface

For elliptical contacts, Hertzian theory is used to calculate the normal force for a given deflection. In order to enable rapid calculation, the approximation formulas given by Brewe and Hamrock [12] are used:

$$F_\mathrm{N} = \pi \kappa E' \sqrt{\frac{\varepsilon\, R'}{4.5} \left(\frac{\delta}{\mathcal{F}}\right)^3} \qquad \textit{(Eq. 5)}$$

with the semi-axis ratio

$$\kappa = \frac{a}{b} \approx 1.0339 \left(\frac{R_x}{R_y}\right)^{0.636}, \quad \textit{(Eq. 6)}$$

the approximated elliptic integrals

$$\varepsilon \approx 1.0003 + 0.5968 \left(\frac{R_y}{R_x}\right), \quad \textit{(Eq. 7)}$$

$$\mathcal{F} \approx 1.5277 + 0.6023 \ln\left(\frac{R_x}{R_y}\right), \quad \textit{(Eq. 8)}$$

the semi-axes of the contact area a and b, the contact's relative principal curvatures R_x and R_y, its effective radius R' and effective Young's modulus E'. Formulas for E' and R' are provided in the nomenclature.

3.1.3. Line Contacts at Roller-Roller and Roller-Race Interface

Hertzian theory does not provide a load-deflection relationship for line contacts. Therefore, a great variety of different relationships were developed over time. A good overview is given for example by Teutsch and Sauer [11]. As recommended by Houpert [13], the approach of Tripp [14] is used.

It follows

$$\delta_i = \left(\frac{2F_N}{\pi l}\right) \cdot \left[\frac{(1-\nu_1^2)}{E_1}\left(\ln\frac{4R_1}{a} - \frac{1}{2}\right) + \frac{(1-\nu_2^2)}{E_2}\left(\ln\frac{4R_2}{a} - \frac{1}{2}\right)\right] \quad \textit{(Eq. 9)}$$

for deflection at the inner ring and

$$\delta_o = \left(\frac{2F_N}{\pi l}\right) \cdot \left[\frac{(1-\nu_1^2)}{E_1}\left(\ln\frac{4R_1}{a} - \frac{1}{2}\right) + \frac{(1-\nu_2^2)}{E_2}\left(\ln\frac{2t}{a} - \frac{\nu_2}{2(1-\nu_2)}\right)\right] \quad \textit{(Eq. 10)}$$

for deflection at the outer ring. Roller-roller contacts are modelled according to eq. 10, since they are also non-conformal contacts.

It should be noted, that Tripp's equations (eq. 9 and 10) cannot explicitly be solved for F_n from a given deflection δ. Yet, a time-consuming iterative solution of the load-deflection relationship is not suitable for MBS. Therefore, a parameter fit with fitting parameters $k_1$and k_2 was performed similarly to Houpert [13] for the roller-roller, roller-outer ring and roller-inner ring contacts:

$$F_n = \frac{l}{k_1} \cdot \delta^{\frac{1}{k_2}}. \quad \textit{(Eq. 11)}$$

3.2. Tangential Force F_t

The resultant tangential friction forces are calculated by weighing the contributions of boundary and elastohydrodynamic lubrication (EHL) regime.

3.2.1 EHL Friction Force F_{EHL}

In this section, the governing equations and assumptions for calculation of the EHL tangential force F_{EHL} are presented.

It is assumed, that the contact area dimensions and the pressure distribution within this area can be modelled using Hertzian formulas. Given the maximum contact pressure p_0, the pressure distribution equals

$$p(x,y) = p_0 \sqrt{1 - \left(\frac{x}{a}\right)^2 - \left(\frac{y}{b}\right)^2} \quad \textit{(Eq. 12)}$$

with

$$p_0 = \frac{1.5\, F_n}{\pi\, a\, b} \quad \textit{(Eq. 13)}$$

for elliptical contacts [15]. The semi-axes of the contact area a and b are calculated using the approximation equations of Brewe and Hamrock [12]:

$$a = \left(\frac{6\,\kappa^2 \varepsilon\, F_N\, R'}{\pi\, E'}\right)^{1/3} \quad \textit{(Eq. 14)}$$

$$b = \left(\frac{6\,\varepsilon\, F_N\, R'}{\pi\, \kappa\, E'}\right)^{1/3}. \quad \textit{(Eq. 15)}$$

For line contacts, pressure distribution equals

$$p(x) = p_0 \sqrt{1 - \left(\frac{x}{a}\right)^2} \quad \textit{(Eq. 16)}$$

with

$$p_0 = \frac{2\, F_n}{\pi\, a\, l} \quad \textit{(Eq. 17)}$$

as the maximum contact pressure. l represents the length of the line contact, which here equals the slice width. Width of the semi-axis a can be calculated via

$$a = \sqrt{\frac{8\, F_n\, R'}{\pi\, E'\, l}}. \quad \textit{(Eq. 18)}$$

Given the pressure distribution, the pressure-induced viscosity increase across the contact area is calculated using Roelands equation [16]:

$$\eta(p,T) = \eta_p \left(\frac{\eta_0(T)}{\eta_p}\right)^{\left(\frac{p_p - p}{p_p}\right)^Z} \quad \textit{(Eq. 19)}$$

with universal parameters $\eta_p = 0.0631$ mPas and $p_p = -196$ MPa.

Base viscosity at ambient pressure η_0 follows from the Vogel equation

$$\eta_0(T) = A \exp\left(\frac{B}{C+T}\right) \qquad \textit{(Eq. 20)}$$

with fluid parameters A, B, C.

A homogenous and constant body mass temperature T is assumed for all elements of the REB. This temperature is then used for calculation of the base viscosity η_0. Liu et al. [17] showed, that using the mass temperature is superior to using the supplied oil temperature.

Shear-thinning of the fluid is considered within the simulation by using a Carreau model. For the shear stress τ follows:

$$\tau = \dot{\gamma}\eta \left(1 + \left(\frac{\eta\dot{\gamma}}{\tau_0}\right)^2\right)^{\frac{n-1}{2}}. \qquad \textit{(Eq. 21)}$$

The shear rate $\dot{\gamma}$ can be approximated as the ratio of relative tangential velocity u_{rel} and central film height h_{c}:

$$\dot{\gamma} = \frac{\partial u}{\partial z} \approx \frac{u_{\mathrm{rel}}}{h_{\mathrm{c}}} = \frac{u_2 - u_1}{h_{\mathrm{c}}}. \qquad \textit{(Eq. 22)}$$

Central film height h_{c} is used instead of the minimum film height, since it represents the major of the contact area and the high pressure area in the contact's center.

For calculation of h_{c}, the dimensionless parameters listed in tab. 1 are introduced. A definition of the required physical input quantities is provided in the nomenclature.

Table 1: Dimensionless parameters used for calculation of film height

Line	Elliptical	
$H = \frac{h}{R'}$	$H = \frac{h}{R_{\mathrm{x}}}$	*(Eq. 23)*
$G = \alpha_{\mathrm{p}}^* E'$		*(Eq. 24)*
$U = \frac{\eta_0 u_0}{E' R'}$	$U = \frac{\eta_0 u_0}{E' R_{\mathrm{x}}}$	*(Eq. 25)*
$W = \frac{F_{\mathrm{n}}}{E' R' l}$	$W = \frac{F_{\mathrm{n}}}{E' R_{\mathrm{x}} l}$	*(Eq. 26)*
$\widetilde{U} = 2\,U$		*(Eq. 27)*
$\widetilde{H} = H \cdot \widetilde{U}^{-0.5}$		*(Eq. 28)*
$M = W \cdot \widetilde{U}^{-0.5}$		*(Eq. 29)*
$L = G \cdot \widetilde{U}^{-0.25}$		*(Eq. 30)*

The viscosity-pressure coefficient α_p^* of the material parameter G (eq. 24) is calculated as proposed by Block [18], [19]:

$$\alpha_{\mathrm{p}}^* = \left(\int_{0.1\,\mathrm{MPa}}^{\infty} \frac{\eta(p = 0.1\,\mathrm{MPa})}{\eta(p)} \mathrm{d}p \right)^{-1} \qquad \textit{(Eq. 31)}$$

Since the integral of eq. 31 cannot be solved analytically for the pressure-viscosity dependence stated in eq. 19, it needs to be solved numerically. In order to avoid a time consuming iterative determination during the MBS, a curve fit of its temperature dependency is performed [20]:

$$\alpha_p^*(T) = c_1 \exp(c_2 T) + c_3 \exp(c_4 T). \qquad \textit{(Eq. 32)}$$

Film height for line contacts is calculated according to the formula proposed by Moes [21]:

$$\widetilde{H}_c = \left[\left(\widetilde{H}_{\mathrm{IR}}^{\frac{7}{3}} + \widetilde{H}_{\mathrm{IE}}^{\frac{7}{3}} \right)^{\frac{3s}{7}} + \left(\widetilde{H}_{\mathrm{PR}}^{-\frac{7}{2}} + \widetilde{H}_{\mathrm{PE}}^{-\frac{7}{2}} \right)^{-\frac{2s}{7}} \right]^{\frac{1}{s}} \qquad \textit{(Eq. 33)}$$

with

$$\widetilde{H}_{\mathrm{IR}} = 3\,M^{-1} \qquad \textit{(Eq. 34)}$$

$$\widetilde{H}_{\mathrm{IE}} = 2.62105\,M^{-0.2} \qquad \textit{(Eq. 35)}$$

$$\widetilde{H}_{\mathrm{PR}} = 1.28666\,L^{\frac{2}{3}} \qquad \textit{(Eq. 36)}$$

$$\widetilde{H}_{\mathrm{PE}} = 1.31106\,M^{-0.125}\;L^{0.75} \qquad \textit{(Eq. 37)}$$

$$s = 0.2\left[7 + 8\,exp\left(-2\frac{\widetilde{H}_{\mathrm{IE}}}{\widetilde{H}_{\mathrm{IR}}}\right)\right]. \qquad \textit{(Eq. 38)}$$

Roller-roller contacts are an especial case, since they exhibit counter rotation, which results in very small to negligible entrainment velocities. Even though no fluid film is expected for zero entrainment velocities (ZEV) according to eq. 33, experiments and numerical EHL-simulations show the existence of such a fluid film [22]. This lubricant film results from a phenomenon referred to as "viscosity wedge": the variation of viscosity across the film thickness due to thermal effects [23]. Even though ZEV contacts are a current field of research [24-26], no universal empirical analytical formula for the film height of line contacts could be derived yet.

Bakolas et al. [27] present simulation results for minimal film heights for ZEV line contacts in the form of data points within a diagram. Aul [27] interpolates these data points, to obtain a rudimentary film height equation for ZEV line contacts:

$$H = [(g_1^{-0.7} + g_2^{-0.7})^{-1.43s} + (g_3^{-1.45} + g_4^{-1.45})^{-0.69s}]^{\frac{1}{s}} \qquad \textit{(Eq. 39)}$$

with

$$g_1 = 0.51\,M^{-0.09} \qquad \textit{(Eq. 40)}$$

$$g_2 = 5.5\,M^{0.5} \qquad \textit{(Eq. 41)}$$

$$g_3 = 0.06\,L^{1.395} \qquad \textit{(Eq. 42)}$$

$$g_4 = 1.04\,M^{0.95}L^{0.08} \qquad \textit{(Eq. 43)}$$

$$s = 0.092\left(9.1 + 10\exp\left(-2\,\frac{g_3}{g_2}\right)\right) \qquad \textit{(Eq. 44)}$$

For calculation of the speed parameter U $\mathrm{u}_0 = \frac{1}{2}(|u_1| + |u_2|)$ is used for the entraining speed.

Within the simulation both film heights from eq. 33 and eq. 39 are calculated and the greater is then used for calculation of the shear rate $\dot{\gamma}$ (eq. 22). While this method is not yet established in literature, upon the author's knowledge, it is the best currently available published method to model ZEV film thickess of line contacts at system level.

The film height formula proposed by Chittenden et al. is used for elliptical contacts [28]:

$$H_c = 4.31\, G^{0.49}\, U^{0.68}\, W^{-0.073}(1-\beta) \qquad \textit{(Eq. 45)}$$

with

$$\beta = \exp\left(-1.23\left(\frac{\frac{R_y}{R_x}\sin^2\xi + \cos^2\xi}{\sin^2\xi + \frac{R_y}{R_x}\cos^2\xi}\right)^{\frac{2}{3}}\right) \qquad \textit{(Eq. 46)}$$

and ξ as the angle between the direction of entrainment velocity and the major axis of the contact ellipse (see fig. 4).

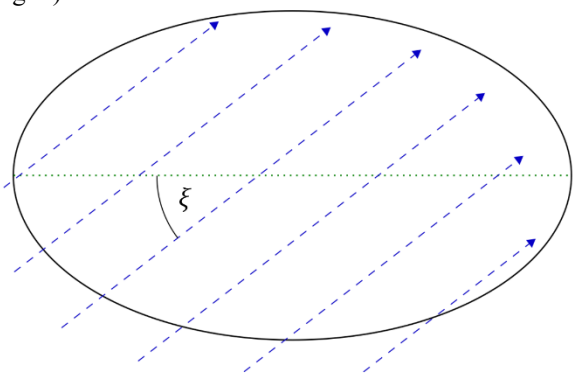

Figure 4: Sketch of the angle ξ between the ellipse's major axis (dotted) and the entrainment velocity field (dashed).

It is assumed, that all contacts are fully-flooded and therefore, no starvation effects on the film height are taken into account. Furthermore, it is anticipated, that shear-thinning and fluid compression can be neglected for calculation of the central film height.

The stated film height formulas in eq. 33 and eq. 45 are only valid for isothermal contacts. Thermal effects are considered using the thermal correction factor ϕ_{th} proposed by Pandey and Gosh for line contacts [29]:

$$\phi_{\mathrm{th}} = \frac{1}{1 + 0.133 \cdot \mathcal{L}^{0.71} \cdot (1 + 5.65 \cdot S^{0.96})} \qquad \textit{(Eq. 47)}$$

with the thermal load parameter

$$\mathcal{L} = \left(-\frac{\partial \eta}{\partial T}\frac{u_0^2}{\lambda_{\mathrm{F}}}\right), \qquad \textit{(Eq. 48)}$$

slide-to-roll-ratio (SRR)

$$S = \frac{u_{\mathrm{rel}}}{u_0} = \frac{2\,(u_2 - u_1)}{u_1 + u_2} \qquad \textit{(Eq. 49)}$$

and λ_{F} as the lubricant's thermal conductivity.

Zhu [30] states, that no thermal correction models are available for elliptical contacts. Therefore, it is assumed, that eq. 47 can also be used as a hypothetical approach for elliptical contacts.

Shear stresses within a fluid cannot exceed a certain, shear-rate-independent, value. This upper boundary is commonly referred to as the limiting shear stress (LSS) τ_{L}. In this paper, the bilinear, temperature-independent, approach of Wang [31] is used for modeling of LSS:

$$\tau_{\mathrm{L}}(p) = \begin{cases} \chi\,(p - p^*) + \tau_{\mathrm{L},0} & \text{if } p < p^* \\ \tau_{\mathrm{L},0} & \text{if } p \geq p^*. \end{cases} \qquad \textit{(Eq. 50)}$$

The final step in calculation of the EHL tangential force F_{EHL} is integration of shear stress distribution over the contact area. Due to the large number of interacting and partially piecewise equations required for calculation of shear stress, an analytical solution of the integral cannot be determined.

Therefore, shear stress is integrated numerically. To ensure an efficient integration, a combination of Gauss-Legendre quadrature and trapezoidal rule is used.

3.2.4. Boundary Friction Force F_{B}

Boundary friction is modelled as Coulomb Friction:

$$F_{\mathrm{B}} = \mu_{\mathrm{B}}\, F_{\mathrm{N}}\, \mathrm{sgn}(u_{\mathrm{rel}}). \qquad \textit{(Eq. 51)}$$

For small SRR, micro slip occurs in an unlubricated contact [32]. The boundary coefficient of friction μ_{B} increases with increasing slip until macro-slip predominates in the contact and μ_B reaches a constant value.

In order to incorporate this phenomenon in the simulation, a simplified model is used. The boundary coefficient of friction μ_B increases linearly with S until a critical value S_0 is reached and remains constant afterwards:

$$\mu_{\mathrm{B}}(S) = \begin{cases} \frac{S}{S_0}\,\mu_{\mathrm{B},0} & \text{if } S < S_0 \\ \mu_{\mathrm{B},0} & \text{if } S \geq S_0. \end{cases} \qquad \textit{(Eq. 52)}$$

In case of small relative and mean velocities, the numerical behavior of F_{B} is undesired, due to abrupt changes of sign of F_{B} (see fig. 5). In order to improve numerical stability, F_{B} is smoothened for $|u_{\mathrm{rel}}| \ll 1$ as shown in fig. 5.

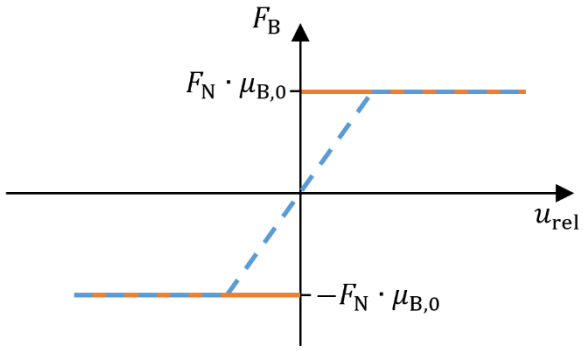

Figure 5: Plot of physical (solid) and smoothened (dashed) boundary coefficient of friction μ_B against relative velocity u_{rel} for $S > S_0$.

3.2.5. Load Sharing in Mixed Lubrication

Mixed and EHL regime are considered. For mixed lubrication the contributions of boundary and EHL regime are weighed using the contact load ratio ϕ according to Zhou and Hoeprich [33]:

$$\phi = \exp\left(-B_{ZH} \cdot \Lambda^{C_{ZH}}\right) \qquad \textit{(Eq. 53)}$$

and

$$F_t = \phi \cdot F_B + (1 - \phi) \cdot F_{EHL}. \qquad \textit{(Eq. 54)}$$

3.3. Rolling Resistance

In addition to friction forces due to relative motion as described in section 3.2., rolling resistance is also considered. Rolling resistance is caused by many physical effects, such as adhesion, hysteresis effects due to plastic deformation, micro-slip, fluid compression in the inlet zone or inlet shear. It creates a torque acting against the direction of rotation.

Since the main kinematic condition of roller-roller and roller end-flange contacts is sliding, rolling resistance is not considered for these contacts.

Similar to calculation of tangential forces, effective rolling resistance is calculated by weighing the contributions of boundary and EHL rolling resistance according to Zhou and Hoeprich [33] (eq. 53 & 54). Boundary rolling resistance due to hysteresis effects for line contacts is calculated via [15]

$$M_B = \alpha_V F_N \frac{2l}{3\pi}. \qquad \textit{(Eq. 55)}$$

EHL rolling resistance is modelled according to Biboulet and Houpert [31]:

$$M_{EHL} = 1.42 \cdot E' R' l R \tilde{U}^{0.5} W^{0.5} \psi \qquad \textit{(Eq. 56)}$$

with

$$\psi = \left(1 + \left(0.966 W^{0.5} \tilde{U}^{-0.25}\right)^{10}\right)^{-0.1}. \qquad \textit{(Eq. 57)}$$

Thermal effects are considered by applying the thermal correction factor from eq. 47 to eq. 56.

4. Benchmarking Study

The performance comparison is conducted by comparing a full-complement cylindrical bearing (bearing B1) simulation (see fig. 6) using the authors' new semi-analytical approach [1] and the gradient method introduced by Koch [9].

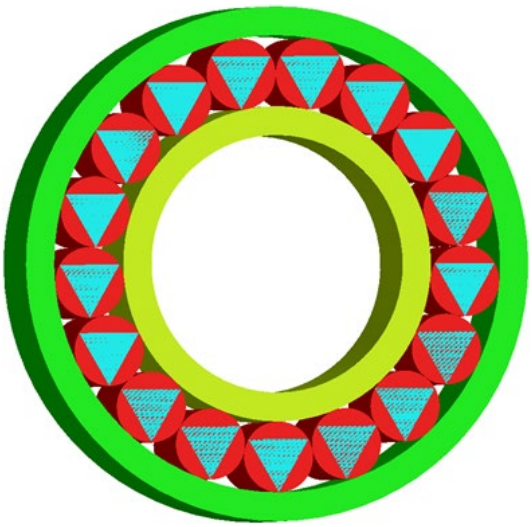

Figure 6: Simulation setup – triangles on rollers are for visualization during post-processing only.

The roller edge is modelled as a torus and the roller end by a convex sphere with high radius in order to represent a plane. The flange is modelled as a cone bounded by two tori at its edges. A sketch of the geometrical approximation can be seen in fig. 1.

The most relevant geometrical parameters are given in tab. 2.

The bearing is lubricated with the reference mineral oil FVA3 and constant radial and axial loads are applied. The relevant lubricant and operating parameters are given in tab. 3. Further lubricant properties can be found in [35].

The simulation includes ramp-up of radial and axial forces, and of the rotational speed of the inner ring. Simulation ends, after two full rotations of the rollers around the bearing at full speed. Inner ring rotation is only allowed in axial direction, while the outer ring is fixed in space. This configuration is chosen to represent a bearing mounted on a very stiff shaft. The rollers are given all six DOF.

For better performance of Koch's method [9], the solution of the contact detection step was stored and used as the initial guess for the iterative contact detection algorithm in the following time step.

Table 2: Load and lubricant parameters of B1

Radial load	Axial load	Rotational speed	Temp.	Viscosity @ 40 °C
5000 N	1000 N	500 rpm	80 °C	81 mPas

Table 3: Geometrical parameters of B1

No. of Rollers	Inner Diameter	Outer Diameter	Opening Angle Flange	Minor Radius TO Roller	Radius Sphere Roller
17	20 mm	29 mm	0.11 °	0.5 mm	5000 mm

5. Results and Discussion

5.1. Precision

Inspection of calculated contact points and theoretical penetration throughout the simulation only reveals differences between the gradient method and the semi-analytical approach within numerical tolerance. Consequently, differences in the resultant forces and torques and consequent kinematics of both simulations are negligible. The identical values for contact points and penetrations throughout the simulation show the equivalence of both methods in terms of precision and are a strong indication for correct implementation of both methods.

It is of high interest, to investigate, which basic figures used for modeling of roller end and flange (see fig. 1) actually got in contact throughout the simulation (see fig. 8 and fig. 9) in order to evaluate detailedness of the geometrical approximation.

It can be seen, that contact between the torus used for modeling the roller and the cone of the respective flange is predominant for both inner (TO-CO_{IR} in fig. 8) and outer ring (TO-CO_{OR} in fig. 9), especially in the load zone. If tilting of the inner ring (IR) is allowed, than other contact pairs occur more often. Herein, tilting refers to a rotational displacement perpendicular to direction of axial and radial force.

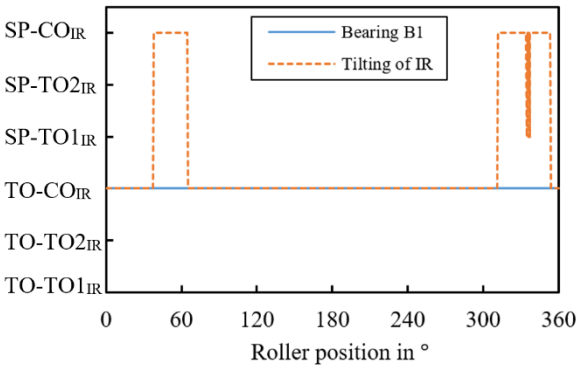

Figure 8: Contact pairings at IR during simulation with and without tilting of IR enabled. For definitions of contact pairs see fig. 1.

This shows, that the simplified geometrical approximation of Gupta [8] in form of a torus and a cone, is a good geometrical approximation. Nevertheless, a more detailed geometric approximation is justified as well. It improves the simulation quality even further, especially in the load-free zone. This is particularly important, since maximum roller slip is determined within the load free zone.

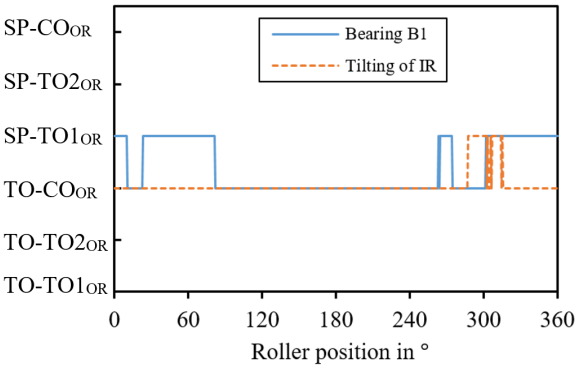

Figure 9: Contact pairings at outer ring during simulation with and without tilting of IR enabled. For definitions of contact pairs see fig. 1.

5.2. Simulation Results

Contact detection models allow incorporation of axial loads into MBS and investigation of their effects on REBs. In this section, some possible applications are presented.

For example, in fig. 10 the bearing frictional torque of B1 is plotted for different constant axial loads. It can be seen, that the bearing frictional torque increases with increasing axial force. This effect can be explained, by increasing friction forces at the flanges (fig. 11).

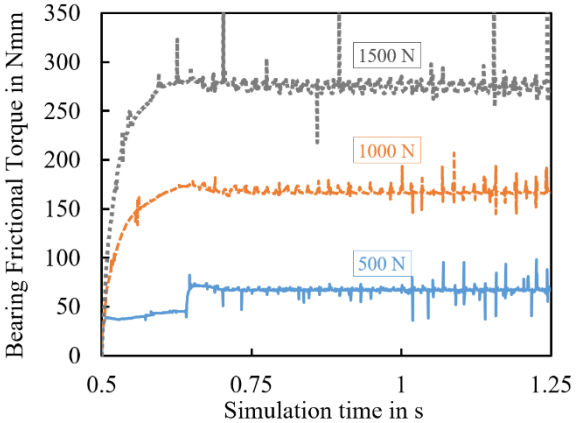

Figure 10: Bearing frictional torque over time for different axial loads. Inner ring rotation ramp-up occurs between 0.5 s and 0.7 s.

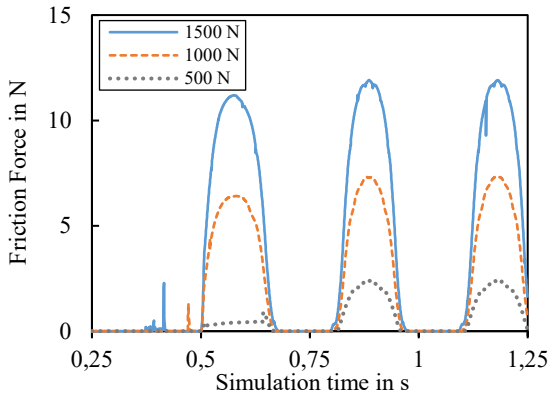

Figure 11: Flange friction force for a single roller over time for different axial loads. Inner ring rotation ramp-up occurs between 0.5 s and 0.7 s.

Furthermore, it can be seen, that the major proportion of the axial force is absorbed by rollers in the load zone (see fig. 12).

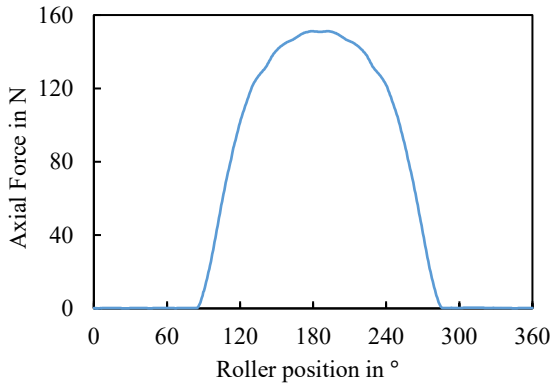

Figure 12: Axial force of a single roller for bearing B1 over roller location.

Radial displacement of inner ring and a positive flange opening angle (see fig. 1 and tab. 3) result in less space in axial direction being left for the rollers within the load zone. Therefore, theoretical penetration and axial load are significantly higher within the radial load zone.

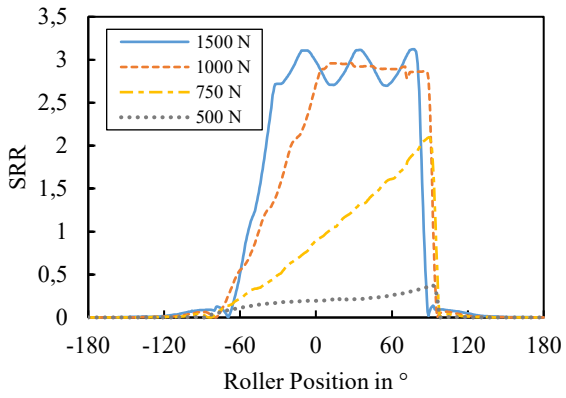

Figure 13: SRR at inner ring over roller position for different axial loads.

Roller slip is the major kinematic effect causing spontaneous non-fatigue damage in REBs, e.g. smearing. The effect of different axial loads on the SRR of rollers can also be studied using the discussed contact detection algorithms (see fig. 13).

5.3. Runtime

The semi-analytical approach reduces runtime of the simulation described in sect. 4 by 35 % compared to a simulation using the gradient method. Therefore, it is shown, that numerical efficiency advantages are still significant, when the new approach is applied within a MBS.

As stated in the introduction, contact detection is just one among many other steps within the MBS of REBs. It is suspected, that its strong impact on the numerical performance results from the large amount of contacts to be evaluated:

Each roller has two possible contact points at the inner flange and two more at the outer flange. Due to the chosen geometrical approximation, for each contact (see fig. 1) six combinations of geometrical figures must be evaluated. Since the bearings consists of 17 rollers, this leads to $17 \cdot 4 \cdot 6 = 408$ contact pairs to be evaluated at each time step.

Numerical performance could be enhanced even further by reducing the number of contacts to be evaluated. Critical analysis of the required complexity of geometrical approximation and of the theoretical possible contact pairs can easily increase numerical performance without the need for new contact detection algorithms.

An example for theoretical impossible contact pairs can be constructed for the geometrical approximation of fig. 1: If the minor radius of the roller's torus is sufficiently large enough and the minor radius of the flange's lower torus is small enough, than no contact between the lower torus and the roller can occur in reality. The roller would get in contact with the cone first and therefore, the number of contacts to be evaluated could be reduced by one third to $17 \cdot 4 \cdot \mathbf{4} = 272$ contacts.

If no change of sign occurs for the axial force, then contact only occurs at the diagonally opposite flanges of inner and outer ring. In this case, the number of evaluated roller end-flange contacts, can be reduced by another 50 %.

Runtime of the gradient method greatly depends on the number of iterations, which are necessary for solving the 8x8 non-linear system of equations. Small differences between the initial guess and solution reduce the number of iterations. Since the solution of the previous time step is used as initial guess of the current time step, it is expected, that runtime of the gradient method is dependent on the step size Δt. Runtime of the contact detection with the gradient

method should be lower for smaller step sizes, since the interim changes of roller and ring spatial displacement become smaller as well.

In order to investigate this hypothesis, the maximum allowed step size $\Delta t_{\max}$ of the simulation is varied and the corresponding relative runtime advantages are plotted in fig. 14.

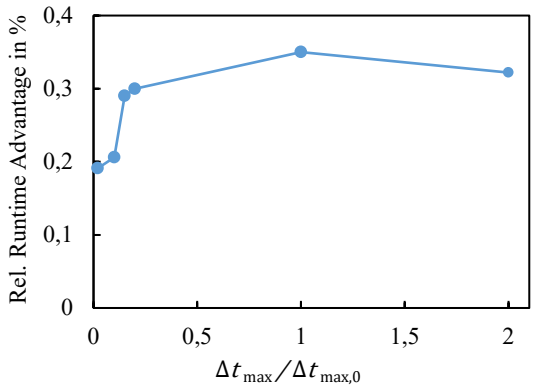

Figure 14: Influence of maximum step size $\Delta t_{\max}$ on runtime advantage of semi-analytical approach. $\Delta t_{\max,0}$ equals the maximum step size with the lowest overall runtime for both methods.

It can be seen, that the runtime advantages are lower for very small time steps. This can be explained, by the lower number of iterations of the gradient method and the independence of the semi-analytical approach from the step size. This insight is relevant, since for relatively stiff systems (e.g. REB with high viscosity oil) a smaller time step size is used within the simulation.

It can be seen, that the new semi-analytical approach's runtime is always lower for realistic maximum step sizes. Even smaller maximum step sizes than shown in fig. 14 lead to unacceptable high total simulation times and were not investigated.

5.4. Practical Consquences in Application of the Semi-Analytical Model

Setting of the first initial guesses of the iterative scheme by Koch [9] at the beginning of the simulation can be quite complex and should not be underestimated. If these values are not chosen correctly, the algorithm does not only converge to a false solution at the first time step (see fig. 2). It is also likely to falsely converge in the following time steps, since the wrong solution will be used as the initial guess of the following time step.

Furthermore, calculation of good initial guesses is especially difficult, if the initial state of the rollers includes skewing and tilting. Accordingly, end users of the MBS must be familiar with the concept of the gradient method.

In addition, concept development for storage of previous solutions should take into account the possibility of race hazard risks.

None of the listed drawbacks exists for the semi-analytical approach [1], though it cannot be ignored, that the gradient method can more easily be extended to include additional basic figures (e.g. polynomials, ellipsoids).

6. Conclusion

The recently developed semi-analytical approach [1] for rapid detection of roller end-flange contacts was compared to the gradient method of Koch [9] for application within a MBS of full-complement cylindrical REB. The bearing simulation includes all six DOF for rollers and rings. Its physical model includes fluid behavior and considers both fluid and mixed lubrication.

Possible applications of dynamic REB simulation were shown and simulation results were presented.

Comparison of the contact detection methods focused on useability, runtime and quality of results.

Main findings of the comparison are:

- There is no compromise in accuracy by using the semi-analytical model [1], since it yields the same trajectories of forces and kinematics as the gradient method [9].
- A more detailed geometrical approximation (see fig. 1) than the torus-cone combination used by Gupta [8] is justified. Fig. 8 and fig. 9 show the occurrence of contacts based on additional combinations of basic figures.
- Application of the semi-analytical approach within MBS reduces runtime of dynamic simulations of REBs compared to the gradient method.
- Runtime advantages are significant (35 % for reference simulation).
- Time step size has an influence on relative runtime advantage. Relative advantages decline for smaller time step sizes.
- The semi-analytical approach has a higher numerical stability, which results in facilitated applicability of the MBS in development processes. Unlike for the gradient method, no knowledge of the working principle of the used contact detection method is required by the end user.

Acknowledgments

The authors would like to thank Prof. Dr. Gerhard Poll (University of Hannover) for helpful and in-depth discussions on modeling of the fluid behavior. Patrick Stuhler, Dr. Nadine Nagler (both Bosch Rexroth AG) and Dr. Timo Kiekbusch (Robert Bosch GmbH) are acknowledged for their general advice on the topic of roller element bearings.

Bibliography

[1] Wolf, M., Sanner A. and Fatemi, A., 2020, "A Semi-Analytical Approach for Rapid Detection of Roller-Flange Contacts in Roller Element Bearings," Proc. Inst. Mech. Eng., Part J.

[2] Wheeler, J.D., 2016, "Non-Elliptical Point Contacts: the Torus-on-Plane Conjunction," Ph.D. thesis, INSA Lyon.

[3] Wheeler, J.D., Fillot, N., Vergne, P., Philippon, D. and Morales-Espejel, G.E., 2016, "On the crucial role of ellipticity on elastohydrodynamic film thickness and friction," Proc. Inst. Mech. Eng., Part J, 230(12), pp. 1503-1515.

[4] Doki-Thonon, T., Fillot, N., Vergne, P. and Morales-Espejel, G., 2012, "Numerical insight into heat transfer and power losses in spinning EHD non-Newtonian point contacts," Proc. Inst. Mech. Eng., Part J, 226(1), pp. 23-35.

[5] Doki-Thonon, T., Fillot, N., Morales-Espejel, G., Querry, M., Phillipon, D., Devaux, N. and Vergne, P., 2013, "A Dual Experimental/Numerical Approach for Film Thickness Analysis in TEHL Spinning Skewing Circular Contacts," Tribol. Lett., 50, pp. 115-126.

[6] MSC Software, 2018, "Adams 2018.1: Online Help," MSC Software, Newport Beach, CA.

[7] Gottschalk, S., Lin, M.C. and Manocha, D., 1996, "OBBTree: A Hierarchical Structure for Rapid Interference Detection," 23rd International Conference on Computer Graphics and Interactive Techniques, Association for Computing Machinery, New Orleans, LA, pp. 171-180.

[8] Gupta, P.K., 1984, Advanced Dynamics of Rolling Elements, Springer-Verlag New York, New York.

[9] Koch, O., 2008, „Dreidimensionale Simulation von kombiniert belasteten Radialzylinderrollenlagern," Ph.D. thesis, Ruhr University Bochum.

[10] Eberly, D., 2019, "Distance to circles in 3D," from https://www.geometrictools.com/Documentation/DistanceToCircle3.pdf

[11] Teutsch, R. and Sauer, B., 2004, "An Alternative Slicing Technique to Consider Pressure Concentrations in Non-Hertzian Line Contacts," Journal of Tribology, 126(3), pp. 436-442.

[12] Brewe, D.E. and Hamrock, B.J., 1977, "Simplified Solution for Elliptical-Contact Deformation Between Two Elastic Solids," Journal of Lubrication Technology, 99 (4), pp. 485-487.

[13] Houpert, L., 2000, "An Engineering Approach to Hertzian Contact Elasticity - Part I," Journal of Tribology, 123(3), pp. 582-588.

[14] Tripp, J. H., 1985, "Hertzian Contact in Two and Three Dimensions," 2473, National Aeronautics and Space Administration (NASA), Cleveland, OH.

[15] Johnson, K.L., 1985, Contact Mechanics, Cambridge University Press, Cambridge.

[16] Hamrock, B.J., Schmid, S.R. and Jacobson, B.O., 2004, Fundamentals of Fluid Film Lubrication, 2nd ed., Marcel Dekker, Inc., New York.

[17] Liu, H.C., Zhang, B.B., Bader, N., Guo, F., Poll, G., and Yang, P., 2019, "Crucial role of solid body temperature on elastohydrodynamic film thickness and traction," Tribology International, 131, pp. 386-397.

[18] Blok, H., 1963, "Inverse Problems in Hydrodynamic Lubrication and Design Directives for Lubricated Flexible Surfaces," International Symposium on Lubrication and Wear, U.S. Atomic Energy Division, Houston, TX.

[19] Vergne, P. and Bair, S., 2014, "Classical EHL Versus Quantitative EHL: A Perspective Part I - Real Viscosity-Pressure Dependence and the Viscosity-Pressure Coefficient for Predicting Film Thickness," Tribol. Lett., 54(1), pp. 1-12.

[20] Fruth, T., 2018, "Vom tribologischen Modellversuch zum Maschinenelement," Ph.D. thesis, University of Kaiserslautern.

[21] Moes, H., 2000, Lubrication and Beyond, University of Twente, Enschede.

[22] Meziane, B., Vergne, P., Devaux, N., Lafarge, L., Morales-Espejel, G.E. and Fillot, N., 2020, "Film Thickness Build-Up in Zero Entrainment Velocity Wide Point Contacts," Tribology International, 141.

[23] Cameron, A., 1958, “The Viscosity Wedge,” ASLE Transactions, 1 (2), pp. 248-253.

[24] Wong, P.L., Zhao, Y. and Mao, J., 2018, “Facilitating effective hydrodynamic lubrication for zero-entrainment-velocity contacts based on boundary slip mechanism,” Tribology International, 128, pp. 89-95.

[25] Zhang, B. and Wang, J., 2016, “Enhancement of thermal effect in zero entrainment velocity contact under low surface velocity,” Proc. Inst. Mech. Eng., Part J, 230(12), pp. 1554-1561.

[26] Zhang, B., Wang, J., Omasta, M. and Kaneta, M., 2016, “Variation of surface dimple in point contact thermal EHL under ZEV condition,” Tribology International, 94, pp. 383-394.

[27] Aul, V., 2014, “Kontaktmodelle zur dynamischen Simulation vollrolliger Zylinderrollenlager,“ Ph.D. thesis, University of Kaiserlslautern.

[28] Chittenden, R. J., Dowson, D., Dunn, J.F., Taylor C.M. and Johnson, K.L., 1985, “A theoretical analysis of the isothermal elastohydrodynamic lubrication of concentrated contacts. II. General case, with lubricant entrainment along either principal axis of the Hertzian contact ellipse or at some intermediate angle,” Proceedings of the Royal Society of London. A. Mathematical and Physical Sciences, 397(1813), pp. 271-294.

[29] Pandey, R. K. and Ghosh, M. K., 1996, “Thermal effects on film thickness and traction in rolling/sliding EHL line contacts - an accurate inlet zone analysis,” Wear, 192(1), pp. 118-127.

[30] Zhu, D., 2013, Encyclopedia of Tribology, Springer, Boston, MA, Chap. Thermal Reduction of EHL Film Thickness.

[31] Wang, D., 2015, “Berechnung der Wälzlagerreibung aufgrund weiterentwickelter rheologischer Fluidmodelle,” Ph.D. thesis, University of Hannover.

[32] Poll, G., 1983, “Der Einfluss der realen Systemeigenschaften auf die Kraftschlussgesetze bei wälzender Relativbewegung,” Ph.D. thesis, Technische Hochschule Aachen.

[33] Zhou, R.S. and Hoeprich, M.R., 1991, “Torque of Tapered Roller Bearings”, Journal of Tribology, 113(3) , pp. 590-597.

[34] Biboulet, N. and Houpert, L., 2010, "Hydrodynamic force and moment in pure rolling lubricated contacts. Part 1: Line contacts," Proc. Inst. Mech. Eng., Part J, 224(8), pp. 765-775.

[35] Laukotka, E.M., 2007, “Referenzölkatalog,” 660, Forschungsvereinigung Antriebstechnik (FVA), Frankfurt am Main.

Nomenclature

Latin Letters

a, b	Semi-axes of contact ellipse
A, B, C	Vogel-parameters
$B_{\mathrm{ZH}}, C_{\mathrm{ZH}}$	Parameters for mixed lubrication
c_i	Fitting parameters for α_{p}^{*}
E	Young's modulus
$E' = 2\left(\frac{1-\nu_1^2}{E_1}+\frac{1-\nu_2^2}{E_2}\right)^{-1}$	Effective Young's modulus
F_{EHL}	EHL friction force
F_{B}	Boundary friction force
F_i	Implicit function of surface *i*
F_{n}	Normal force
F_{t}	Tangential force
G	Material parameter
h_c	Central fluid film height
H	Film height parameter
k_i	Fitting parameters of load-deflection relationship
l	Length of line contact
$\mathcal{L}$	Thermal load parameter
M_{B}	Torque of boundary rolling resistance
M_{EHL}	Torque of EHL rolling resistance
n, τ_0	Parameters of Carreau model
p	pressure
$p_{\mathrm{p}}, Z, \eta_{\mathrm{p}}$	Parameters of Roelands equation
p_0	Max. pressure
$\boldsymbol{P}_i$	Contact point *i*
$\boldsymbol{P}_{\mathrm{m}}$	Contact location
$\boldsymbol{r}$	Location vector
R	Radius
$R' = \left(\frac{1}{R_{\mathrm{x}}}+\frac{1}{R_{\mathrm{y}}}\right)^{-1}$	Equivalent Radius
$R_{\mathrm{x}}, R_{\mathrm{y}}$	Relative principle curvatures
S	Slide-to-roll ratio (SRR)
sgn	Sign function
t	Thickness outer ring
T	Body mass temperature
u_i	Velocity of surface *i*
$U, \tilde{U}$	Speed parameters
$u_0 = \frac{u_1+u_2}{2}$	Entraining velocity
u_{rel}	Relative surface velocity
W	Load parameter

Greek Letters

α_p^{*}	Viscosity-pressure coefficient
α_{V}	Coefficient of boundary rolling resistance
$\dot{\gamma}$	Shear rate
δ	Theoretical penetration
Δt	Time step size of simulation

$\Delta t_{\max}$	Maximum time step size of simulation
η	Viscosity
η_0	Viscosity at ambient pressure
$\Lambda = \frac{h_c}{\sigma}$	Film thickness ratio
μ_{B}	Boundary coefficient of friction
ξ	Angle between entrainment velocity and major axis of contact
σ	Composite root-mean-square roughness
τ	Shear stress
τ_{L}	Limiting shear stress (LSS)
ν	Poisson's ratio
ϕ	Load sharing ratio
ϕ_{th}	Thermal correction factor

Indices and Abbreviations

b	Boundary
c	Central
B1	Reference bearing (see sect. 4)
CO	Cone
DOF	Degree of freedom
EHL	Elastohydrodynamic lubrication
IR	Inner ring
LSS	Limiting shear stress
MBS	Multibody dynamics simulation
REB	Roller element bearing
SP	Sphere
SRR	Slide-to-roll-ratio
TO	Torus
OR	Outer ring
ZEV	Zero entrainment velocity